Profiles of near-surface rock mass strength across gradients in burial, erosion, and time

K. F. Townsend[1], M. K. Clark[1], and D. Zekkos[2†]

[1]Department of Earth and Environmental Sciences, University of Michigan, Ann Arbor, MI, USA.

[2]Department of Civil and Environmental Engineering, University of Michigan, Ann Arbor, MI, USA.

Corresponding author: Kirk Townsend (kirkft@umich.edu)

[†]Now at Department of Civil and Environmental Engineering, University of California Berkeley, Berkeley, CA, USA.

Key Points:

- We present a novel approach to quantify near-surface rock mass strength on depth profiles from surface and subsurface measurements
- The rock mass strength of sandstone units increases with increasing maximum burial depth prior to exhumation
- Rock strength and erosion rate are positively correlated, which we suggest is driven by critical zone residence time and weathering extent

Abstract

Rock mass strength is recognized as an important control on landscape morphology and evolution. However, the controls on rock strength in mountainous topography remain poorly characterized, in part because strength remains challenging to quantify at spatial scales relevant to geomorphology. Here we quantify the mechanical properties of rock masses using subsurface S-wave velocities, Schmidt hammer hardness values, and Geological Strength Index (GSI) observations. We produce shallow depth profiles of rock mass shear strength using intact rock hardness as measured from a Schmidt hammer, and assessment of the structure and surface conditions of fractures using GSI. We apply these techniques to the Western Transverse Ranges, southern California, USA, where gradients in stratigraphic age and erosion rate allow us to evaluate our methodology. We resolve strength differences of 200 kPa to ~5 MPa that appear to be related to diagenetic changes associated with the maximum burial depth of young clastic sedimentary rocks. For rocks of the same lithologic type, stratigraphic age, and inferred burial histories, we resolve smaller differences in strength (300 kPa – 1.5 MPa) that appear to be positively correlated with mean erosion rates. We suggest that the increase in strength with increasing erosion rate reflects decreased residence time in the weathering zone for ranges experiencing faster fault slip rates. These findings demonstrate up to an order of magnitude variability in strength with respect to burial, erosion, and time for lithologically similar rocks. As such, lithology alone is unlikely to adequately capture the role of rock strength in landscape evolution.

1 Introduction

Near-surface rock strength is fundamental to topographic form and the erosive processes responsible for landscape evolution (Davis, 1899; Gilbert, 1877). Encompassing soil, weathered and intact rock, the rock mass strength profile extends from the surface to tens of meters depth and exerts a control on the evolution of mountainous landscapes by resisting erosion and contributing to the steepness of hillslopes and river channels (DiBiase et al., 2018; Montgomery & Brandon, 2002; Schmidt & Montgomery, 1995; Townsend et al., 2020a). The processes and rates by which landscapes evolve are sensitive to rock mass strength, which contributes to hillslope stability and failure mechanisms (Collins & Sitar, 2008; Gallen et al., 2015; Hoek & Brown, 1980; Selby, 1980), the architecture of the critical zone (CZ) and weathering processes (St. Clair et al., 2015; Medwedeff et al., 2019; Riebe et al., 2017), and the mechanisms of bedrock erosion in channels (Bursztyn et al., 2015; Forte et al., 2016; Gallen, 2018; Roy et al., 2015; Sklar & Dietrich, 2001). Rock strength is often quantified with laboratory tests on hand-sized samples, but we recognize that fractures and weathering dramatically reduce strength at the spatial scales relevant to geomorphic processes compared to their intact counterparts (Hoek & Brown, 1980; Schmidt & Montgomery, 1995; Townsend et al., 2020a). Laboratory approaches may overestimate near-surface rock strength at outcrop, hillslope, or regional spatial scales by an order of magnitude or more (Bunn et al., 2020; Gallen et al., 2015; Schmidt & Montgomery, 1995), yet adequately accounting for variability of rock mass strength in landscape evolution is challenged by the paucity of approaches for quantifying in-situ strength at the relevant spatial scales (Gallen et al., 2015; Schmidt & Montgomery, 1995; Townsend et al., 2020a).

Many efforts to model landscape evolution in mountainous terrain incorporate rock strength as an erodibility coefficient (e.g. 'K' in the stream power erosion model) that is typically

estimated or assigned by lithologic type (Bursztyn et al., 2015; Stock & Montgomery, 1999). Although lithologic type is widely recognized to contribute to the strength of intact (i.e. unfractured) rock pieces (e.g. Sklar & Dietrich, 2001), recent studies have focused on quantifying the effect of fracture density and saprolite weathering on rock mass strength at geomorphically relevant spatial scales, which can be influenced by climatic and tectonic gradients (Gallen et al., 2015; Kirkpatrick et al., 2020; J. A. Marshall & Roering, 2014). Fracture generation and weathering are sensitive to a number of environmental factors, including climate (Gabet et al., 2010; Gallen et al., 2015; Goudie, 2016), tectonics (DiBiase et al., 2018; Kirkpatrick et al., 2020; Molnar et al., 2007; Neely et al., 2019), burial depth of sedimentary rocks (Townsend et al., 2020a), and geomorphic position on the landscape (Gabet et al., 2015; Leone et al., 2020; Medwedeff et al., 2019; Slim et al., 2015). Quantifying the relationships between these environmental variables and fracturing, weathering, and the resultant rock mass strength at appropriate spatial scales will further our ability to accurately model the evolution of active mountainous regions with respect to strength.

Active tectonic settings may present a paradox that challenges a simple view that weaker rocks erode faster than stronger rocks. On the one hand, active tectonism and bedrock uplift increase the density of fractures, thereby facilitating pathways for weathering in the subsurface and producing detachable blocks that are easily transported by surface processes (DiBiase et al., 2018; Dühnforth et al., 2010; Molnar et al., 2007; Scott & Wohl, 2018). This results in a reduction in rock mass strength and is associated with an increase in erodibility and in erosion rates (Roy et al., 2016). However, under steady-state conditions wherein the rate of climate-modulated erosion is balanced with the rate of rock uplift (Hack, 1975; Willett & Brandon, 2002), landscapes adjust to variability in rock strength through changes in slope, rather than erosion rate (Korup, 2008). In this case, active tectonism leading to increased erosion rates may lead to steeper slopes with reduced soil thickness and shorter residence times of rock masses in the CZ (Dixon et al., 2012; West et al., 2005). Reduced CZ residence leads to a decrease in the rate and extent of chemical weathering, thereby increasing the near-surface rock strength profile. These relationships are likely modulated by lithologic type, climate, and inheritance of fractures from earlier tectonic events, and variability in tectonic setting and history also likely influence bedrock fracture patterns. Untangling these competing influences on rock mass strength will require new approaches for quantifying scale-dependent strength while controlling for lithologic type, climate, and other factors that influence strength in the near-surface environment.

In this study, we present a novel approach to evaluating near surface strength profiles (up to 30 m depth) from surface and subsurface measurements. We assess strength at broad spatial scales (10s of meters) that extend ~15 to 40 m depth in the subsurface. Because soil thickness is thin (<50 cm) in our study area, our measurements largely represent the strength of fresh to weathered bedrock and saprolite. Using short geophysical arrays (< 80 m in length), we measure subsurface velocities of S-waves, which are a measure of the stiffness of rock masses (Barton, 2006). Stiffness is influenced by porosity, density, and elastic moduli, which vary with both weathering extent and degree of lithification of sedimentary rocks (Barton, 2006; Leung & Radhakrishnan, 1990; Vilder et al., 2019; Von Voigtlander et al., 2018), allowing us to use seismic velocities to explore these variables across environmental gradients. At outcrop sites, we use a Schmidt hammer to quantify hardness of intact rock blocks between fractures, and we assess the density, orientation, and surface conditions (i.e. weathering) of fractures with Geological Strength Index (GSI) observations (Hoek & Marinos, 2000). To aggregate the

contributions of the intact (unfractured) strength, and the outcrop-scale fracture characteristics, we apply the Hoek & Brown criterion to quantify outcrop-scale shear strength as a function of depth (Hoek et al., 2002; Hoek & Brown, 1980, 1997). These approaches average subsurface rock strength over the relatively large spatial scales necessary to incorporate the strength-limiting behavior of fractures and discontinuities, which set the upper limit on strength at the outcrop- and hillslope-scales relevant for geomorphic processes (Gallen et al., 2015; Hoek & Brown, 1980, 1997; Townsend et al., 2020a).

2 Geologic Setting

2.1 Sampling Strategy

The unique geologic setting of the Western Transverse Ranges (WTR) of southern California, USA, enables us to isolate many variables that are recognized to affect rock mass strength, including tectonic history, erosion rate, lithologic type, and climate. The WTR contain multiple reverse-fault bounded mountain ranges where rock uplift rates are uniform within individual ranges, but vary from range to range (Niemi & Clark, 2018; Townsend et al., 2018) (Figure 1). Ranges are predominately composed of late-Cretaceous through Plio-Pleistocene age clastic sedimentary rocks that were deposited during multiple stages of regional extension and basin formation (Namson & Davis, 1988) (Figure 1 and Figure 2). Original burial depths in these Cenozoic basins range from < 1 km to up to 10 km, and corelative stratigraphic units are exposed in the individual ranges today. Because faults of the WTR are moving at different rates (S. T. Marshall et al., 2013), we interpret variable mean erosion rates across three studied ranges that are quantified by geochemical methods (Niemi & Clark, 2018; Portenga et al., 2017; Townsend et al., 2018). Lithologic types are similar throughout, and precipitation today is uniform across the region. Therefore, the WTR field area offers the ability to investigate the effect of burial and erosion histories on the mechanical properties and strength of rock masses while isolating for lithologic type and climate.

The ease at which our novel approach can be deployed in the field allows for broad spatial sampling across the study area. We quantify rock mass mechanical properties across regional gradients in subsidence and exhumation histories, as well as mean erosion rates measured over two different timescales. To explore the affect of variable basin history on rock mass strength, we focus on the Topatopa Mountains on the northern boundary of the WTR (Figure 1). We then explore the affect of mean erosion rates by focusing on correlative stratigraphic units in the Topatopa Mountains, Santa Monica Mountains, and northern Channel Islands (Figure 1).

2.2 Burial and Exhumation Gradient in the Topatopa Mountains

Exposures of Late-Mesozoic to Cenozoic sedimentary rocks in the Topatopa Mountains allow us to investigate the affect of differential burial depths under constant rock uplift rates. The Topatopa Mountains expose more than 10 km of stratigraphic section of Plio-Pliestocene through Cretaceous age sedimentary rocks in a broad homocline that dips to the east with strike perpendicular to the range front (Dibblee, 1982) (Figures 2, S1-4). Here, mapped geologic units are of a similar lithologic type (primarily clastic sedimentary rocks and predominately sandstones) but vary in maximum burial depth as a function of geologic age (i.e. stratigraphic

interval). These rocks are being exhumed due to active reverse faulting along the San Cayetano Fault (Figure 1 and Figure 2), which initiated in the west during late-Miocene time and propagated eastward through Pliocene time, causing an increase in rock exhumation (i.e. structural relief) from west to east across the range while maintaining uniform uplift rates along strike of the fault (Rockwell, 1988; Townsend et al., 2018).

The Plio-Pleistocene Saugus Formation, exposed on the eastern end of the range (Figure 2), is the stratigraphically highest unit and has not been buried by additional sediments, providing a constraint on the maximum burial depth of underlying units in this continuous stratigraphic section (DeVecchio et al., 2012). Using this constraint, the Oligocene Sespe Formation was buried by up to 5-7 km of overlying sedimentary rocks prior to being exhumed, with stratigraphically higher units experiencing less burial prior to exhumation (Dibblee, 1991, 1993; Townsend et al., 2020a). The Cretaceous sediments at the bottom of the section were buried by as much as 7-10 km of overlying sediments during final basin formation prior to inversion by activity on the San Cayetano Fault. Because the range has a simple tectonic history of basin inversion, we can neglect the influence of deformation inherited from earlier tectonism.

2.3 Regional Differences in Erosion Rate

The Topatopa Mountains, Santa Monica Mountains, and northern Channel Islands share two mapped stratigraphic units, the Miocene Monterey Formation and the Oligocene Sespe Formation. The Oligocene Sespe Formation exhibits less regional variability in lithology compared to the Monterey Formation. Deposited in a broad coastal plain, the Sespe Formation is predominately a deltaic and fluvial unit composed of medium- to coarse-grained sandstones with occasional conglomerate and shale interbeds, and is often identified by distinctive red beds (Howard, 1988). The unit outcrops in the central Topatopa Mountains north of Fillmore, CA, the central Santa Monica Mountains north and east of Malibu, CA, and southern Santa Rosa Island (Figure 2). By targeting the Sespe Formation in each location, we can isolate and assess the contribution of erosion rate to rock strength while controlling for stratigraphic age, original burial depth, and lithologic type. Despite these efforts, we acknowledge that additional uncharacterized variables may systematically vary within the Sespe Formation across our study area, including but not limited to mineraology, composition of cements, degree of diagenesis, porosity, and hydrologic conductivity.While the Miocene Monterey Formation is ubiquitous across central and southern California, significant lateral facies variation within our study area precludes use of this unit for comparisons of erosion rates. The unit varies from medium-grained sandstones (locally known as the Modelo Formation) in the Topatopa Mountains to a fine-grained diatomaceous shale in the Santa Monica Mountains and northern Channel Islands (Dibblee, 1982; Gordon, 2014).

Erosion rates in the Topatopa Mountains, Santa Monica Mountains, and northern Channel Islands are quantified over two timescales from low-temperature thermochronology (Niemi & Clark, 2018; Townsend et al., 2018) and [10]Be cosmogenic radionuclides (Hughes, 2019; Portenga et al., 2017). Low-temperature (U-Th-Sm)/He thermochronometers are sensitive to tectonic and geomorphic processes affecting the upper crust, and the resultant time-temperature data provide constraints on the timing and rates of burial and subsequent erosion of inverted sedimentary basins over Myr to tens of Myr timescales (e.g. Ehlers, 2005). Apatite (U-Th-Sm)/He ages represent the time since a sample cooled below ~40-80°C, which occurs at

depths of 2-4 km, assuming typical geothermal gradients (Farley, 2002; Flowers et al., 2009). Ages from the higher-temperature zircon (U-Th)/He thermochronometer represent the time since a sample cooled below ~180-200°C at depths of 5-8 km (Farley, 2002; Reiners et al., 2002). Ages from paired thermochronometers, and/or multiple samples of one thermochronometer with vertical (stratigraphic or elevation) separation, can be inverted for million-year averages in erosion rate over several million years (Farley, 2002).

Apatite (U-Th-Sm)/He thermochronometry ages throughout the WTR generally range from late-Miocene to Pleistocene, implying recent and rapid rock exhumation (Niemi & Clark, 2018; Townsend et al., 2018). We observe variability in apatite (U-Th)/He ages, which are youngest in the Topatopa Mountains (1.3 to 4.5 Ma), older in the Santa Monica Mountains (2 to 7 Ma), and oldest from Santa Rosa Island (6 to 8 Ma) (Niemi & Clark, 2018; Townsend et al., 2018). Inverse thermal modelling of these data reveal gradients in cooling rates, and by assuming a geothermal gradient of 30 °C/km, exhumation rates of 1.2 to 1.6 mm/yr since 3 Ma are inferred for the central Topatopa Mountains, 0.7 to 1.0 mm/yr since 5 Ma are inferred in the central Santa Monica Mountains, and a slower rate of 0.3 mm/yr since ~10 Ma is inferred for Santa Rosa Island (Niemi & Clark, 2018; Townsend et al., 2018).

Basin-wide erosion rates that integrate over shorter time intervals of 10^2-10^3 years are calculated using ^{10}Be cosmogenic radionuclide concentrations in quartz. In-situ cosmogenic radionuclides are produced in minerals near the earth's surface by secondary cosmic radiation bombarding atomic nuclei (Granger et al., 1996). The cosmic ray flux decreases exponentially with depth below the surface, so the surface concentration of cosmogenic radionuclides is indirectly proportional to the erosion rate (von Blanckenburg, 2005). By measuring concentrations of cosmogenic radionuclides in stream sediments, a spatially-averaged erosion rate for the entire upstream catchment can be produced (von Blanckenburg, 2005; Granger et al., 1996). Two samples from the central Topatopa Mountains yield erosion rates of 1.92 mm/yr and 2.21 mm/yr, respectively (Hughes, 2019), whereas samples from five catchments in the central Santa Monica Mountains yield erosion rates ranging from 0.23 mm/yr to 0.36 mm/yr (Portenga et al., 2017). Published data for ^{10}Be cosmogenic radionuclide concentrations from the northern Channel Islands is not available.

Over both thermochronometric (10^5-10^6 years) and cosmogenic (10^2-10^3 years) integration time scales, erosion rates are higher in the Topatopa Mountains than in the Santa Monica Mountains. The differences in erosion rates are interpreted to reflect differences in the rate of fault slip on the San Cayetano Fault and the Malibu Coast Fault, respectively (Niemi & Clark, 2018; Portenga et al., 2017; Townsend et al., 2018). GPS velocities confirm the relative difference in fault slip rate between the two ranges, albeit at higher overall rates during this shorter timescale of 10^0-10^1 years (S. T. Marshall et al., 2013, 2017). Dip-slip motion on the San Cayetano Fault and the Malibu Coast Fault are estimated at 5.4 ± 1.7 mm/yr and 1.1 ± 0.8 mm/yr, respectively, which also imply relatively faster tectonically-driven erosion rates in the Topatopa Mountains than in the Santa Monica Mountains.

2.4 Climate

The climate is characterized as Mediterranean, with generally warm, dry summers, and cool, wet winters. Mean annual precipitation across the study area is similar, with weather

stations at the base of the Topatopa Mountains reporting 45 to 54 mm/yr, and stations at the base of the Santa Monica Mountains reporting 40 to 62 mm/yr (WRCC, 2020), although rainfall is likely greater at higher elevations due to orographic effects. Mean annual precipitation reported from the one station on Santa Rosa Island is 29 mm/yr (WRCC, 2020).

3 Methods

3.1.1 Seismic Surveys

Shallow seismic surveys with short arrays and active sources are inexpensive, non-invasive, and portable, which make them adventageous for study of hillslope environments in mountainous topography (Befus et al., 2011; St. Clair et al., 2015; Flinchum et al., 2018; Von Voigtlander et al., 2018). Such surveys also aggregate material properties over larger spatial scales than other field testing methods, such as dynamic penetration tests, shear vane or point load testing, or laboratory approaches that measure uniaxial or triaxial compressive strength. S-wave velocity profiles are typically used in geotechnical engineering because shear wave velocities (Vs) are related to the low-strain shear modulus (G) such that $G = \rho Vs^2$, where ρ is the material density. Thus, subsurface propagation velocities of shear waves are a measure of stiffness of rock and soil and can be representative of the shear strength of the material. Shear wave velocities are also sensitive to the density of fractures and void spaces at multiple scales, such that a decrease in porosity and increase in density are expected with diagenetic changes associated with lithification of sedimentary rocks, resulting in an increase in stiffness and seismic velocities with increasing lithification. Conversely, an increase in porosity, decrease in density, and mineralogic changes associated with degree of weathering, contribute to a decrease of seismic velocities as weathering progresses (Barton, 2006). For example, typical S-wave speeds for fresh crystalline, unfractured bedrock are >1500 m/s, and a progressive reduction in seismic velocities to 300 m/s occurs from fresh bedrock to weathered or fractured bedrock, saprolite, and the near-surface disaggregated layer (mobile regolith, soils, and grus) (Martin & Diehl, 2004).

While it is possible to measure shear wave velocities directly, it requires three-component geophones that are expensive and time consuming to install (Park et al., 1999). Thus approaches using surface (Rayleigh) waves from multi-channel vertical-component arrays to interpret S-wave velocity profiles are commonly applied to geotechnical investigations because Rayleigh waves travel at 90% of the speed of shear waves (Anbazhagan & Sitharam, 2009; Park et al., 1999, 2000). These approaches rely on dispersion of Rayleigh waves, which occurs when the elastic properties of the near-surface changes with depth. Typically, lower frequency (or longer wavelength) waves travel at faster speeds because they sample higher velocity material at greater depths (Stokoe & Santamarina, 2000). Surface waves are also adventagous over P-wave profiles recently used in geomorphology studies (St. Clair et al., 2015; Clarke & Burbank, 2011; Holbrook et al., 2014) because of a low sensitivity to pore fluid content and the ability to interpret velocity inversions with depth.

Here we applied the multichannel analysis of surface waves (MASW) approach, in which an impulsive source and linear array of geophones are used to generate shot records, which are transformed to velocity-frequency relationships and then used in a forward modeling approach to produce Vs profiles as a function of depth (Park et al., 1998, 1999). Resolution is highest in the shallowest part of each profile, and the ability to resolve velocity decreases with depth because

lower-frequency waves sample deeper material, which averages more of the subsurface (Stokoe & Santamarina, 2000). Both fundamental and higher-mode Rayleigh waves were considered in the analysis. Higher-mode Rayleigh waves can arise when low-velocity layers are interbedded with high-velocity layers (Stokoe et al., 1994), and utilizing higher modes is needed to better constrain and characterize these complex subsurface velocity structures (Xia et al., 2003).

3.1.2 Seismic Acquisition and Processing

Seismic data was recorded using a 16-channel Geometrics ES-3000 portable seismometer (12 profiles), and a 24-channel Geometrics Geode portable seismometer (48 profiles), using 4.5 Hz geophones spaced at 1.5 to 3 m intervals. Impulsive sources were produced by striking a 25-cm square, 5-cm thick plastic plate with a 7.2 kg sledge hammer, and shots were stacked 8-10 times to improve the signal-to-noise ratio. Shots were produced from the end of the array at an offset of 15-20% of the total array length to avoid near-field effects (Yoon & Rix, 2009). Total line lengths varied from 53 to 78 m, producing S-wave velocity profiles with typical depths of investigation of 15 to 45 m. At 10 sites, a second survey was recorded with a smaller geophone spacing of 0.7 to 1.0 m in order to increase the resolution of the S-wave velocity profile near the surface. These shorter surveys were centered over the midpoint of the longer array.

We generated S-wave velocity profiles using Geometrics SeisImager/SW software (Pickwin Version 5.2.1.3, WaveEq Version 4.0.1.0, 2016). Initial velocity structures with 30 layers were assumed for each site, and the maximum depth of each profile was set to half the longest measured wavelength. Dispersion curves were back-calculated from initial velocity profiles and compared against the measured dispersion curve. The difference between the observed and theoretical dispersion curves is described using the root mean square error (RMSE), which provides a means to assess the inverted velocity models. S-wave velocity profiles were iteratively adjusted by manually changing the velocity of each layer in order to minimize the RMSE between observed and theoretical dispersion curves. The best-fit dispersion curve matches were used to produce the final S-wave velocity profiles. It should also be noted that inversion of surface wave dispersion curves for S-wave velocity profiles is a non-unique solution, as multiple S-wave velocity profiles may produce similar theoretical dispersion curves (Foti et al., 2009). Geologic considerations, other site data, and judgment are commonly applied to derive a "best-estimate" S-wave velocity profile.

3.1.3 Calculation of V_{s30}

V_{s30} is a common parameter used in seismically active regions to characterize seismic site response and is defined as the time-averaged shear-wave velocity to 30 m depth (Borcherdt, 2012). V_{s30} is calculated by dividing the total thickness of each profile by the total travel time, wherein travel time is the summation of the thickness divided by velocity of each layer. For the 38 (of 60) sites for which S-wave profiles do not reach 30 m, V_{s30} was approximated following the approach of Wang & Wang (2015) using equation 1.

(1) $$\log V_s(30) = \log V_s(z_2) + \frac{\log 30 - \log z_2}{\log z_2 - \log z_1}[\log V_s(z_2) - \log V_s(z_1)]$$

Where $V_s(z_1)$ and $V_s(z_2)$ are the time-averaged shear-wave velocities to depths z_1 and z_2, respectively. Equation 1 interpolates Vs between z_1 and z_2, and then extrapolates to z = 30 m.

With $z_1 = 10$ m and z_2 set to the maximum depth of each profile, we approximate V_{S30}. We chose this approach because it is more likely to yield accurate V_{S30} for individual sites than methods that rely on empirically-derived coefficients (e.g. Boore, 2004), which may be regionally dependent (Boore, 2004; Wang & Wang, 2015). Although dispersion curves are to some degree non-unique to a specific S-wave velocity profile, it has been shown that the final S-wave velocity profile and specific location of low-velocity layers has little effect on V_{S30} of individual sites (Garofalo et al., 2016).

3.2 Shear Strength Depth Profiles using the Hoek and Brown Criterion

Shear strength (τ) is defined as the maximum shear stress that a material can sustain before failure, and is controlled by a number of variables, including porosity, mineralogy and the composition of interstitial cements and the structure and surface condition of fractures (Selby, 1993). Shear strength varies as a function of confining (normal) stresses, and the increase in shear strength with increasing confining stress defines the failure envelope in shear stress versus normal stress space (Hoek & Brown, 1997). We initially calculate shear strength at the surface from an outcrop, where the confining stress is zero. By then relating the confining stress to lithostatic earth pressure (Jaky, 1944; Mayne & Kulhawey, 1982), we calculate shear stress as a function of depth into the shallow subsurface, thereby enabling quantification of material strength over a depth interval that is relevant to geomorphic processes and facilitating direct comparison to measured subsurface S-wave velocities.

Rock mass strength (i.e. outcrop-scale) can be effectively estimated with ranked classification schemes that reduce the intact rock strength (i.e. the strength of the rock mass between fractures) by the structure and surface conditions (weathering) of discontinuities in the larger outcrop (Hoek & Brown, 1980, 1997; Selby, 1980). The Hoek and Brown criterion has an advantage over other rank classifications such as Selby (1980, 1993) because it was developed to quantify the strength and behavior of fractured rock masses for use in geotechnical engineering appliations using empirical calibrations. For a fractured rock mass, the ability of intact blocks to slide and rotate within a rock mass under varying stress conditions is controlled by the shape of the blocks, as well as the conditions of the surfaces separating the blocks (Hoek & Brown, 1997). A key input to the Hoek & Brown criterion is the Geological Strength Index, or GSI, of Hoek & Marinos (2000). GSI is a framework that ranks rock masses on a scale of 0 to 100 based on six classes of structure and five classes of discontinuity surface conditions, with low values reflecting highly fractured and weathered discontinuities, and high values reflecting unfractured, unweathered discontinuities. Where GSI = 100 (no or widely spaced discontinuities), the shear strength of the associated rock mass is entirely dependent on the parameters used for the intact

strength of the rock blocks. GSI observations, typically over a range of ± 5, were recorded from each site in the field (Townsend et al., 2020b).

We specifically use the Hoek & Brown (2002) criterion, which empirically derives and predicts a non-linear increase in the maximum effective principal stress at failure with increasing minimum principal effective stress using equation 2.

(2) $$\sigma'_1 = \sigma'_3 + \sigma_{ci}\left(m_b\frac{\sigma'_3}{\sigma_{ci}} + s\right)^a$$

Where σ_1' is the maximum principal effective stress at failure, σ_3' is the minimum principal effective stress at failure, and σ_{ci} is the uniaxial compressive strength of the intact rock blocks (Hoek et al., 2002). m_b is defined by equation 3,

(3) $$m_b = m_i \exp\left(\frac{GSI-100}{28-14D}\right).$$

Where m_i is a material constant dependent on lithologic type, and D is the disturbance factor. m_b is effectively the material constant (m_i) reduced by GSI; where GSI = 100, $m_b = m_i$. We define m_i using values for each lithologic type in Table 2 of Hoek & Brown (1997). We set D = 0.7, the value used for excavations, as most outcrops studied are roadcuts (Hoek et al., 2002).

S and a are constants for each rock mass and are defined by equations 4 and 5 (Hoek et al., 2002).

(4) $$S = \exp\left(\frac{GSI-100}{9-3D}\right)$$

(5) $$a = \frac{1}{2} + \frac{1}{6}\left(e^{-GSI/15} - e^{-20/3}\right)$$

Shear strength is related to the principal stresses by equation 6

(6) $$\tau = (\sigma'_1 - \sigma'_3)\frac{\sqrt{d\sigma'_1/d\sigma'_3}}{\sigma'_1/\sigma'_3 + 1}$$

Where $d\sigma_1$'/σ_3' is given by equation 7

(7) $$d\sigma'_1/d\sigma'_3 = 1 + am_b(m_b\sigma'_3/\sigma_{ci} + s)^{a-1}$$

For the shear strength calculation, we assume σ_3' to be the horizontal confining stress at a given depth interval, defined by equation 8

(8) $$\sigma'_3 = K_0\rho gz$$

Where K_0 is the coefficient of lateral earth pressure at-rest, ρ is the rock mass density (set constant at ρ = 2300 kg/m^3), g is gravitational acceleration (g = 9.8 m/s^2), and z is depth below the surface. K_0 is related to the friction angle of the materials, and typically varies from ~0.5 for clayey materials with low friction angle at undrained conditions, to ~0.1 for intact rock masses

with high friction angle (Jaky, 1944; Mayne & Kulhawy, 1982). Sandy soils and fractured rock masses typically yield intermediate values of ~0.25 to ~0.45 (Jaky, 1944; Mayne & Kulhawey, 1982), and here we set $K_0 = 0.35$ constant.

At each site where GSI observations were recorded, relative intact rock hardness of unfractured blocks was measured in-situ using a Schmidt hammer (Original Schmidt, type N, manufactured by Proceq; Townsend et al., 2020b). This is a spring-loaded device that measures rebound values that scale with laboratory measurements of uniaxial compressive strength (UCS) (Aydin & Basu, 2005; Selby, 1993). Due to rock heterogeneity and analytical variability of the Schmidt hammer, we calculated mean rebound-values (R) from 20 measurements taken from a horizontal position of the least fractured rock surface at each site. The rock surface was cleared of any debris prior to recording Schmidt hammer measurements, but was otherwise not altered. We removed any measurement that yielded a hollow sounding impact or fractured the rock, and all measurements of <10 were recorded as 0. We converted Schmidt hammer rebound values into uniaxial compressive strength using the regression from Deere & Miller (1966) (Equation 9).

(9)
$$\sigma_{ci} = \text{UCS} = 6.9 \times 10^{[0.0087\,\gamma\,N+0.16]}$$

Where γ is density (set constant at $\gamma = 2.3$ g/cm^3) and N is the mean Schmidt hammer rebound value R. Although care was taken to ensure that measurements were recorded from relatively fresh, unweathered surfaces, it is important to recognize that near-surface conditions are likely weakened to varying degrees compared to subsurface conditions due to weathering within the near surface environment. As an alternative approach and a confirmation of our analysis, we also generated shear strength profiles using intact rock strength values from R Grade (Table 1 in Hoek et al., 1997) estimates recorded at 30 sites. The R Grade is a relative measure of intact rock strength based on blows to a rock mass from a geologic hammer in the field. R Grade scales from R0 to R6, and for each value, we defined UCS using the midpoint of the range reported in Table 1 of Hoek et al. (1997). For ranges of R Grade values (e.g. R1-R2), we used the UCS value on the Grade boundary. We find that mean values only differ by up to ~15% at the deepest part of the profiles, and that the patterns in shear strength profiles match to those produced using Schmidt R and Equation 9 for this same subset of data (Figure S5). Given this consistency between Schmidt R and R Grade values, we calculate shear strength profiles for the entire field inventory with intact strength defined using Schmidt R field measurements and Equation 9.

We note that shear strength profiles presented here should be considered conservative estimates of the true strength of these materials at depth, due to the likelihood of near-surface weathering, rock mass relaxation, and the assumptions required to project strength curves into the subsurface.

3.3 S-wave Velocity Profiles vs. Shear Strength

We use the common depth axis of both shear wave and shear strength profiles to develop S-wave-shear strength relationships for each survey site where both outcrop observations and Vs surveys were measured. Mean S-wave velocities and shear strength were calculated from binned depth intervals of 3 m from individual S-wave and shear strength profiles. Although S-wave velocities are sensitive to rock mass characteristics, such as rock structure, porosity and type of rock, that also influence the strength of a rock mass, seismic velocities are a measure of stiffness

and not a direct measurement of rock mass strength. Therefore, these relationships enable a direct quantification of strength from seismic velocities.

4 Results

4.1 Lithologic Type

S-wave velocity profiles were produced for 60 sites in the study region, and shear strength profiles were produced from Schmidt hammer R measurements and GSI observations recorded from 210 sites (Figure 2). Vs_{30} across the WTR ranges from 258 to 1441 m/s, mean Schmidt hammer R ranges from 0 to 60, GSI ranges from 10 to 95, and shear strength at 10 m depth ranges from < 0.1 to 10.3 MPa (Townsend et al., 2020b). Intact rock strength is known to vary by lithologic type, among other factors (Sklar & Dietrich, 2001), so we first separate our data into lithologic units (Figure 3 and Figure 4). We observe that mean Schmidt R and GSI is generally higher for clastic sedimentary rocks than igneous (mafic volcanic, volcaniclastic, and granitic) or metamorphic (slate, schist) rocks (Figure 3). The mean shear strength of sandstones specifically is higher than other lithologic types, as is mean Vs_{30} of both shale and sandstone sites, although S-wave velocities for other lithologic types were measured at just a single site (Figure 3). Looking at the S-wave velocity and shear strength profiles directly, we observe that sandstone and shale sites span a wide range, with subsurface S-wave velocities ranging from ~300 to ~1400 m/s, and shear strength ranging from near-zero to 13.6 MPa, whereas other lithologic types generally plot on the lower end of the range of sandstone and shale sites (Figure 4).

4.2 Stratigraphic Age in the Topatopa Mountains

Mean Schmidt R, GSI, shear strength at 10 m depth, and Vs_{30} by mapped geologic formation in the Topatopa Mountains are reported in Table 1. These data were collected from sandstones at different sites within each formation, and $\pm 1\sigma$ represent site-to-site variability in data. We observe that GSI, S-wave velocity profiles, and shear strength profiles increase with increasing stratigraphic age (Figure 5). When separated into individual stratigraphic units, mean Schmidt R values from the Plio-Pleistocene Saugus Formation at the top of the stratigraphic section are generally < 10, but reach 48 ± 11 at the base of the section in the unnamed Cretaceous unit (Table 1, Figure 6). Schmidt R is a measure of the hardness of intact rock blocks and not outcrop-scale strength, but we also observe that both GSI and Vs_{30} increase over this same interval. GSI values range from 23 in the Plio-Pleistocene section, to 83 ± 8 in the unnamed Cretaceous unit, and Vs_{30} ranges from 361 ± 18 m/s in the Pliocene Pico Formation, to 1092 ± 213 m/s in the Eocene Matilija Formation, indicating that rock mass mechanical properties averaged over spatial scales larger than an intact block also increase over this interval. Collectively, we observe a consistent increase in all strength metrics and S-wave velocities with increasing stratigraphic age from the Plio-Pleistocene through Oligocene units (Figure 6).

Strength metrics and S-wave velocities from different sites within the Eocene and Cretaceous section are generally higher than the Plio-Pleistocene through Oligocene stratigraphic units, but data from different sites within these units also exhibit more variability within one standard deviation (Figure 5 and Figure 6). Notably, the mean Vs_{30} of the Eocene Coldwater and Juncal fms. is ~300 m/s slower than stratigraphically lower and higher units (Table 1 and Figure

6), which is mirrored by mean GSI values. However, mean Schmidt R values from different sites within the Eocene and Cretaceous units are nearly the same (Figure 5), which may suggest relatively consistent and high intact strength despite variability in strength at the larger spatial scales reflected by the GSI and S-wave velocity data.

4.3 Sespe Formation

Mean strength metrics and Vs_{30} of Sespe Formation sandstone sites in the Topatopa Mountains, Santa Monica Mountains, and Santa Rosa Island are reported in Table 2. Mean Schmidt R, GSI, shear strength at 10 m depth, and Vs_{30} of Sespe Formation sites are higher in the Topatopa Mountains than in the Santa Monica Mountains, although mean GSI, shear strength, and Vs_{30} overlap within one standard deviation (Table 2). Schmidt R and GSI were collected from just one Sespe Formation site on Santa Rosa Island, but each metric is lower than mean values of the Sespe Formation from either the Topatopa Mountains or Santa Monica Mountains (Table 1).

We observe variability of up to ~500 m/s in S-wave velocities in the uppermost 10 m of Sespe Formation sites from both the Topatopa Mountains and Santa Monica Mountains (Figure 7). However, from 10 m to 30 m depth, S-wave velocities of Sespe Formation sites more tightly diverge onto distinct trends of ~800 m/s for the Santa Monica Mountains, and ~1100 m/s in the Topatopa Mountains, and do not overlap within one standard deviation (Figure 7). Likewise, the mean shear strength profile of the Sespe Formation from the Topatopa Mountains is ~0.4 MPa stronger at 5 m depth, and ~0.7 MPa stronger at 30 m depth than the mean profile from the Santa Monica Mountains (Figure 7).

Mean GSI values from Sespe Formation sites are higher in the Topatopa Mountains than the Santa Monica Mountains, but individual values vary from 40 to 85 (Table 2). However, GSI values can be separated into their structural (out of 6) and surface quality (out of five) components to look at the relative contributions of fracturing and weathering, respectively. The mean structure component of Sepse Formation GSI from both ranges is identical (5.0 and 4.9), whereas the mean surface component of Sespe Formation GSI in the Santa Monica Mountains (3.6 ± 0.4) is lower than in the Topatopa Mountains (4.1 ± 0.6) (Table 2), reflecting greater degree of weathering on fracture surfaces.

4.4 S-wave Velocities and Shear Strength

Shear strength versus S-wave velocity are shown in Figure 8. These data include all lithologic types and are separated into four relationships based on geologic age. Data from Pliocene, Miocene, Oligocene, and Eocene through Cretaceous sites define approximately linear trends, with Pliocene data plotting at lower shear strength and S-wave velocities, Miocene and Oligocene data plotting at intermediate values, and Eocene through Cretaceous data plotting at higher shear strength and S-wave velocities (Figure 8). We regressed through these data to produce relationships between shear strength and S-wave velocities (Table 3). These

relationships may provide first-order estimates of S-wave velocities from GSI observations in the study area, if geophysical imaging or borehole data is unavailable (Medwedeff et al., 2019).

5 Discussion

5.1 Comparison to Typical Strength Values

Although all seismic surveys were conducted on rock units, S-wave velocities fall within ranges characteristic of 'stiff soil' (180 to 360 m/s), 'very dense soil and soft rock' (360 to 760 m/s), and 'rock' (760 to 1500 m/s) (Martin & Diehl, 2004). In particular, S-wave velocities from the Pliocene sandstones in the Topatopa Mountains range from ~200 to ~500 m/s despite being similar in composition to Oligocene and Eocene sandstones with S-wave velocities ranging from ~600 to ~1500 m/s, which further highlights the wide variability in rock mass properties within a single lithologic type. No sites from the WTR yield S-wave velocities characteristic of 'hard rock' (>1500 m/s), even at depth (Martin & Diehl, 2004). However, these high velocities are more characteristic of unweathered plutonic rocks than clastic sedimentary rocks (Barton, 2006). Our Vs_{30} values are consistent with bedrock (i.e. non-Quaternary) sites in the WTR from the USGS compilation of Vs_{30} (Yong et al., 2016).

Schmidt hammer rebound values generally fall within the range of very weak rock (10-35), weak rock (35-40), and moderately strong rocks (40-50) (Selby, 1993). Within this classification scheme, mean values from Plio-Pleistocene through Oligocene sandstones in the Topatopa Mountains are very weak, and Eocene and Cretaceous sandstones yield mean values characteristic of weak to moderately strong rocks (Selby, 1993).

5.2 Stratigraphic Age and Burial Depth

The physical and chemical changes associated with lithification and burial in deep sedimentary basins exert a strong control on the strength of sedimentary rockmassses (e.g. Collins & Sitar, 2008). In the Topatopa mountains, both strength and Vs show this expected relationship between increasing strength and seismic velocities with increasing formation age and stratigraphic depth interval. The stratigraphically highest unit (Plio-Pleistocene Saugus Formation) is only weakly cemented and the burial depth of the middle to upper-Miocene section is estimated at ~2-3 km (Townsend et al., 2018, 2020a). The Plio-Pleistocene through Oligocene units are a continuous section, and the Oligocene Sespe Formation at the base of this interval was buried by up to 5-7 km of overlying sedimentary rocks prior to being exhumed (Dibblee, 1991, 1993; Townsend et al., 2020a).

Recently deposited sediments with no overburden are typically loosely packed, highly porous, and have not been cemented. Increases in temperature and pressure during subsequent burial increases grain packing and decreases porosity through both physical and chemical compaction. Chemical compaction enriches pore water with dissolved silica though partial dissolution of minerals, and precipitation of this silica in pore spaces further reduces porosity while adding cements, leading to lithification of the sediments (Boggs Jr., 2011). These physical and chemical changes occur with burial from the surface to at least 5 km depth (Worden & Burley, 2003), which is similar to the thickness of the stratigraphic interval over which we observe the highest increase in Schmidt R, GSI, shear strength, and S-wave velocities with burial

depth (Figure 5 and Figure 6), also consistent with a compaction and lithification gradient. The positive correlation between strength and stratigraphic age is consistent with Townsend et al.'s (*2020*) finding that cohesive strength at spatial scales of both intact samples (direct-shear test) and hillslopes (landslide model estimates) increase as a function of original burial depth, both between and within formations, across the Plio-Pleistocene through Miocene section exposed in the eastern Topatopa Mountains. Geologic time likely also contributes to an increase in the degree of diagenesis and resultant rock strength, but we cannot separate this effect from maximum burial depth (i.e. both stratigraphic age and maximum burial depth covary with strength).

Burial to depths greater than 5 km is unlikely to drive further increased rock strength through lithification and diagenesis (Worden & Burley, 2003). The Oligocene through Cretaceous section in the Topatopa Mountains likely experienced burial to depths of 5-10 km, and although field proxies of rock strength from these units are generally higher than from the overlying Plio-Pleistocene through Oligocene section, they do not demonstrate much further increase in strength with increasing stratigraphic age (Figure 6). Mean values of Schmidt R and GSI are the same across Eocene and Cretaceous units (Figure 6), and mean S-wave velocity profile and mean shear strength profile of all Eocene and Cretaceous units are similar to the means of Oligocene data (Figure 2), although large $\pm 1\sigma$ indicates significant variability about means of both formation-level data (Figure 6) and data binned by stratigraphic age (Figure 5), indicating significant variability in rockmass properties. Specifically, Mean Vs_{30} and GSI from the Juncal Formation are lower than values from overlying and underlying units (Figure 6). The reduced outcrop-scale strength of this unit may be explained by greater tectonic deformation, as Juncal Formation sites are within a complex structural zone where the generally north-south striking, gently east-dipping homocline of the Topatopa Mountains and the predominantly east-west striking, near-vertical homocline of the Santa Ynez Mountains intersect in a major syncline (Dibblee, 1982). At this same structural transition, strain accommodation transitions from the emergent portion of the San Cayetano Fault in the east to multiple blind structures in the west (Dibblee, 1982; Levy et al., 2019). Many hillslopes within this structural transition are mantled in landslides (Gutierrez et al., 2008), likely a consequence of tectonically-weakened bedrock, and we observe in the field that outcrops contain more open fractures than overlying or underlying stratigraphic units.

5.3 Rock Strength and Erosion Rate

Each metric of strength from the Sespe Formation shows a positive correlation with erosion rate, suggesting that rock strength decreases as a function of decreasing erosion rate (Figure 9). Erosion rate differences across these ranges are set by differences in the rate of fault slip and bedrock uplift. There is not a strong gradient in mean annual precipitation across the study area (WRCC, 2020) to explain the variation of weathering by climate differences, so we therefore posit that the decrease in rock mass strength reflects increased weathering due to longer residence times within the near surface environment (CZ) due to slower erosion rates driven by faulting. Although we have not directly quantified soil or bedrock weathering in the WTR, the surface quality axis of GSI observations provides a qualitative measure of the degree of weathering (Hoek & Brown, 1997). Surface quality values from Sespe Formation sites are higher (less weathered) in the Topatopa Mountains than the Santa Monica Mountains, which is in turn higher than the one site from Santa Rosa Island (Table 2). In the San Gabriel Mountains (east of

our study area), increased erosion rates driven by increasing rates of tectonic uplift cause a decrease in the rates and extent of chemical weathering (Dixon et al., 2012). When erosion rates are sufficiently rapid, the extent and rate of weathering becomes limited by the kinetics of weathering reactions, and the decrease in chemical weathering leads to a decrease in soil residence time and soil thickness as weatherable minerals are eroded before they have sufficient time to weather completely (Dixon et al., 2012; West et al., 2005). The length of time that a particular parcel of rock resides in the CZ likely has a direct influence on the degree of weathering, and therefore, the strength of the rock mass once it reaches the surface (Moon & Jayawardane, 2004; de Vilder et al., 2019).

In locations with high weathering efficiency and relatively uniform bedrock lithologic types, S-wave velocities and shear strength may also vary with geomorphic position due to differences in erosion rate, weathering extent, and topographic stresses (St. Clair et al., 2015; Medwedeff et al., 2019). S-wave velocity and shear strength data from ridge and hillslope positions across the WTR are highly variable, but do not demonstrate systematic trends (Figure S7). Channel sites produce faster mean S-wave velocities and higher mean shear strengths than either hillslope or ridge sites (Figure 5), but this observation may be biased by the location of sites in the Eocene and Cretaceous section, which are predominately located near channels due to the inaccessibility of hillslope or ridge sites and the general lack of ridge sites in our study. However, we note that S-wave velocities from one channel site in the Miocene section and one site in the Oligocene section of the Topatopa Mountains plot at the higher end of the range of velocity profiles from hillslope sites (Figure 5), suggesting that the higher confining stress of this topographic position contributes to increased S-wave velocities.

Although we sought to control for stratigraphic age, inferred burial depth, and lithologic type, other factors that influence rock strength may vary systematically with our field sites, including but not limited to: original minerology, composition of interstitial cements, porosity, and hydrogeologic conditions. These datasets are currently unavailable across the study area, and given the correlations presented here, we suggest a weathering control as a plausible mechanism to explain the observed variability in strength. However, we acknowledge that other variables may contribute to the distribution of rock strength in the WTR.

5.4 Santa Ynez Mountains Comparison

Duvall et al. (2004) report Schmidt R values in the western Santa Ynez Mountains (Figure 1) for several stratigraphic units that also outcrop in the Topatopa Mountains. Mean Schmidt R values (± standard error) of the Monterey Formation (34.9 ± 1.0) and Matilija Sandstone (42.1 ± 1.3) from the Santa Ynez Mountains fall within the range of mean values (± 1σ) of sites in these same formations in the Topatopa Mountains (Table 1) (Duvall et al., 2004). However, mean Schmidt R values (± standard error) of the Vaqueros Sandstone (22.7 ± 0.34) and Sespe Formation (20.9 ± 0.35) from the Santa Ynez Mountains are lower than mean values from the same formations in the Topatopa Mountains (Table 1) (Duvall et al., 2004). The thickness of the paleo-basin in the Santa Ynez Mountains is thinner than in the western Topatopa Mountains (Helmold & van de Kamp, 1984), and these differing values may reflect variable basin histories. Alternatively, these lower Schmidt R values may reflect differing weathering extents, as long-term erosion rates inferred from low-temperature thermochronometry

(Townsend et al., 2018), and geodetically-derived modern strain rates (S. T. Marshall et al., 2013) are lower in the Santa Ynez Mountains than the Topatopa Mountains.

5.5 Implications for Landscape Evolution

Landscape evolution models typically incorporate rock strength into a single erodibility parameter (e.g. *K*, Stock & Montgomery, 1999) that is often held fixed as an individual model simulation progresses through time. Data presented here demonstrates quantitatively that rock strength during the early stages of mountain building is instead a dynamic variable that evolves with time. Following initial inversion of a sedimentary basin, reverse faulting elevates poorly-consolidated, mechanically-weak sedimentary rocks, and with continued exhumation, progressively deeper sedimentary rocks with higher rock mass strength are exposed at the surface (Townsend et al., 2020a). This evolving distribution of rock mass strength will likely decrease the erodibility of the overlying landscape, which we expect will impart a signal on the relief structure of the landscape (Montgomery & Brandon, 2002; Schmidt & Montgomery, 1995; Whipple et al., 1999). With continued slip on the range-bounding San Cayetano Fault, we might expect that topographic relief in the eastern Topatopa Mountains, where the Oligocene through Plio-Pleistocene section is currently preserved (Figure 2), will increase through time as stronger stratigraphic units are incrementally exposed at the surface, without requiring an increase in the rate of rock uplift.

We also identify a positive correlation between rock mass mechanical properties and erosion rate, suggesting a decrease in erodibility as erosion rates increase. This observation may be indicative of a negative feedback, wherein an increase in rock mass strength due to increased erosion rates acts to resist further erosion, which in turn provides another mechanism to grow topographic relief. Our results apply to fresh and slightly weathered rock masses, but recent work on soil and saprolite strength demonstrates an increase in strength with increased weathering extent (Heimsath & Whipple, 2019). The relationship between erosion rate and soil/saprolite strength is opposite the relationship we document with rock masses, and suggests that as the strength of rock masses increases with decreased weathering, the strength of the overlying soil actually decreases. This may be one mechanism to explain the reduction in soil thickness with increased erosion rates, but further work will be required to identify and quantify the interdependencies of bedrock strength, erosion rates, weathering, and soil production. These relationships are likely to be influenced by other variables, including local climate, soil production efficiency, and fracture density (Neely et al., 2019), but data presented here provides insight into the behavior and interdependencies of rock mass strength in orogenic systems.

6 Conclusions

Here we apply field based methods for quantifying shear strength depth profiles of the near surface environment relevant for surface processes. We demonstrate that our approach can successfully produce expected patterns in mechanical properties that relate to burial and diagenesis of clastic sedimentary rocks. Or strength profiles also show a consistent relationship with changes in seismic velocity that lends further support to shear strength determinations over a range in values consistent with stiff soil to weak-moderately strong rock (0.1 to 13.6 MPa). We apply these same techniques to rock masses of the same geological age, lithologic type, and inferred burial depth, which outcrop in ranges bounded by faults with differing slip rates. Here

we observe that each metric of rock mass strength is positively correlated with tectonically-driven erosion rates inferred from both catchment-averaged [10]Be cosmogenic radionuclides and low-temperature (U-Th)/He thermochronometry. We posit that the observed increase in strength with increasing erosion rate is a function of lesser weathering due to shorter residence time in the near-surface environment. Such an interpretation challeneges the simplistic notion that fast erosion rates associate with weaker rocks, and highlights to complex role that tectonics and relief may impart on the mechanical evolution of rock to transportable, erodible material.

Data Availability Statement

Raw seismic data (.dat files), dispersion curves, S-wave velocity profiles, and summary files with site information are available from the Deep Blue data repository at https://doi.org/10.7302/krah-yx31. A supplemental document with additional figures is included in Supporting Information.

References

Anbazhagan, P., & Sitharam, T. G. (2009). Spatial variability of the depth of weathered and engineering bedrock using multichannel analysis of surface wave method. *Pure and Applied Geophysics*, *166*(3), 409–428. https://doi.org/10.1007/s00024-009-0450-0

Aydin, A., & Basu, A. (2005). The Schmidt hammer in rock material characterization. *Engineering Geology*, *81*(1), 1–14. https://doi.org/10.1016/j.enggeo.2005.06.006

Barton, N. (2006). *Rock quality, seismic velocity, attenuation and anisotropy*. Boca Raton, FL: CRC press.

Befus, K. M., Sheehan, A. F., Leopold, M., Anderson, S. P., & Anderson, R. S. (2011). Seismic Constraints on Critical Zone Architecture, Boulder Creek Watershed, Front Range, Colorado. *Vadose Zone Journal*, *10*(3), 915. https://doi.org/10.2136/vzj2010.0108

von Blanckenburg, F. (2005). The control mechanisms of erosion and weathering at basin scale from cosmogenic nuclides in river sediment. *Earth and Planetary Science Letters*, *237*(3–4), 462–479. https://doi.org/10.1016/j.epsl.2005.06.030

Boggs Jr., S. (2011). *Principles of Sedimentology and Stratigraphy*. Pearson.

Boore, D. M. (2004). Estimating V̄s(30) (or NEHRP site classes) from shallow velocity models (depths < 30 m). *Bulletin of the Seismological Society of America*, *94*(2), 591–597. https://doi.org/10.1785/0120030105

Borcherdt, R. D. (2012). VS30 – A Site-Characterization Parameter for Use in Paper Title Line Simplified Building Codes, Earthquake Resistant Design, GMPEs, and ShakeMaps. In *15th World Conference on Earthquake Engineering, Lisbon Portugal* (Vol. 10).

Bunn, M., Leshchinsky, B., & Olsen, M. J. (2020). Geologic Trends in Shear Strength Properties Inferred Through Three‑Dimensional Back Analysis of Landslide Inventories. *Journal of Geophysical Research: Earth Surface*, *125*(9), 1–25. https://doi.org/10.1029/2019jf005461

Bursztyn, N., Pederson, J. L., Tressler, C., Mackley, R. D., & Mitchell, K. J. (2015). Rock strength along a fluvial transect of the Colorado Plateau - quantifying a fundamental control on geomorphology. *Earth and Planetary Science Letters*, *429*, 90–100. https://doi.org/10.1016/j.epsl.2015.07.042

St. Clair, J., Moon, S., Holbrook, W. S., Perron, J. T., Riebe, C. S., Martel, S. J., et al. (2015). Geophysical imaging reveals topographic stress control of bedrock weathering. *Science*, *350*(6260), 534–539. https://doi.org/10.1126/science.aab2210

Clarke, B. A., & Burbank, D. W. (2011). Quantifying bedrock-fracture patterns within the shallow subsurface: Implications for rock mass strength, bedrock landslides, and erodibility. *Journal of Geophysical Research: Earth Surface*, *116*(4). https://doi.org/10.1029/2011JF001987

Collins, B. D., & Sitar, N. (2008). Processes of coastal bluff erosion in weakly lithified sands, Pacifica, California, USA. *Geomorphology*, *97*(3–4), 483–501. https://doi.org/10.1016/j.geomorph.2007.09.004

Davis, W. M. (1899). The Geographical Cycle. *The Geographical Journal*, *14*(5), 481–504.

Deere, D., & Miller, R. (1966). *Engineering classification and index properties for intact rock.*

DeVecchio, D. E., Heermance, R. V., Fuchs, M., & Owen, L. A. (2012). Climate-controlled landscape evolution in the Western Transverse Ranges, California: Insights from Quaternary geochronology of the Saugus Formation and strath terrace flights. *Lithosphere*, *4*, 110–130. https://doi.org/10.1130/L176.1

Dibblee, T. W. (1982). Regional geology of the Transverse Ranges Province of southern California. In D. L. Fefe & J. A. Minch (Eds.), *Geology and Mineral Wealth of the Califrnia Transverse Ranges* (pp. 7–26). Santa Ana, California: South Coast Geological Society, Inc.

Dibblee, T. W. (1991). *Geologic Map of the Piru Quadrangle, Ventura County, California*. Santa Barbara, California: Dibblee Geological Foundation.

Dibblee, T. W. (1993). *Geologic Map of the Val Verde Quadrangle, Los Angeles and Ventura Counties, California*. Santa Barbara, California: Dibblee Geological Foundation.

DiBiase, R. A., Rossi, M. W., & Neely, A. B. (2018). Fracture density and grain size controls on the relief structure of bedrock landscapes. *Geology*, *46*(5), 399–402. https://doi.org/10.1130/G40006.1

Dixon, J. L., Hartshorn, A. S., Heimsath, A. M., DiBiase, R. A., & Whipple, K. X. (2012). Chemical weathering response to tectonic forcing: A soils perspective from the San Gabriel Mountains, California. *Earth and Planetary Science Letters*, *323–324*, 40–49. https://doi.org/10.1016/j.epsl.2012.01.010

Dühnforth, M., Anderson, R. S., Ward, D., & Stock, G. M. (2010). Bedrock fracture control of glacial erosion processes and rates. *Geology*, *38*(5), 423–426. https://doi.org/10.1130/G30576.1

Duvall, A. R., Kirby, E., & Burbank, D. W. (2004). Tectonic and lithologic controls on bedrock channel profiles and processes in coastal California. *Journal of Geophysical Research*, *109*(F3), 1–18. https://doi.org/10.1029/2003JF000086

Ehlers, T. A. (2005). Crustal Thermal Processes and the Interpretation of Thermochronometer Data. *Reviews in Mineralogy and Geochemistry*, *58*(1), 315–350. https://doi.org/10.2138/rmg.2005.58.12

Farley, K. A. (2002). (U-Th)/He Dating: Techniques, Calibrations, and Applications. *Reviews in Mineralogy and Geochemistry*, *47*(1), 819–844. https://doi.org/10.2138/rmg.2002.47.18

Flinchum, B. A., Steven Holbrook, W., Rempe, D., Moon, S., Riebe, C. S., Carr, B. J., et al. (2018). Critical zone structure under a granite ridge inferred from drilling and three-dimensional seismic refraction data. *Journal of Geophysical Research: Earth Surface*, *123*(6), 1317–1343. https://doi.org/10.1029/2017JF004280

Flowers, R. M., Ketcham, R. A., Shuster, D. L., & Farley, K. A. (2009). Apatite (U-Th)/He thermochronometry using a radiation damage accumulation and annealing model. *Geochimica et Cosmochimica Acta*, *73*(8), 2347–2365. https://doi.org/10.1016/j.gca.2009.01.015

Forte, A. M., Yanites, B. J., & Whipple, K. X. (2016). Complexities of landscape evolution during incision through layered stratigraphy with contrasts in rock strength. *Earth Surface Processes and Landforms*, *41*(12), 1736–1757. https://doi.org/10.1002/esp.3947

Foti, S., Comina, C., Boiero, D., & Socco, L. V. (2009). Non-uniqueness in surface-wave inversion and consequences on seismic site response analyses. *Soil Dynamics and Earthquake Engineering*, *29*(6), 982–993. https://doi.org/10.1016/j.soildyn.2008.11.004

Gabet, E. J., Wolff-Boenisch, D., Langner, H., Burbank, D. W., & Putkonen, J. (2010). Geomorphic and climatic controls on chemical weathering in the High Himalayas of Nepal. *Geomorphology*, *122*(1–2), 205–210. https://doi.org/10.1016/j.geomorph.2010.06.016

Gabet, E. J., Mudd, S. M., Milodowski, D. T., Yoo, K., Hurst, M. D., & Dosseto, A. (2015). Local topography and erosion rate control regolith thickness along a ridgeline in the Sierra Nevada, California. *Earth Surface Processes and Landforms*, *40*(13), 1779–1790. https://doi.org/10.1002/esp.3754

Gallen, S. F. (2018). Lithologic controls on landscape dynamics and aquatic species evolution in post-orogenic mountains. *Earth and Planetary Science Letters*, *493*, 150–160. https://doi.org/10.1016/j.epsl.2018.04.029

Gallen, S. F., Clark, M. K., & Godt, J. W. (2015). Coseismic landslides reveal near-surface rock strength in a highrelief, tectonically active setting. *Geology*, *43*(1), 11–14.

https://doi.org/10.1130/G36080.1

Garofalo, F., Foti, S., Hollender, F., Bard, P. Y., Cornou, C., Cox, B. R., et al. (2016). InterPACIFIC project: Comparison of invasive and non-invasive methods for seismic site characterization. Part I: Intra-comparison of surface wave methods. *Soil Dynamics and Earthquake Engineering*, *82*, 222–240. https://doi.org/10.1016/j.soildyn.2015.12.010

Gilbert, G. K. (1877). *Report on the geology of the Henry Mountains: Geographical and geological survey of the Rocky Mountain region*. Washington. D.C.

Gordon, G. (2014). *Stratigraphic evolution and architectural analysis of structurally confined submarine fans: A tripartite outcrop-based study*. Colorado School of Mines.

Goudie, A. S. (2016). Quantification of rock control in geomorphology. *Earth-Science Reviews*, *159*, 374–387. https://doi.org/10.1016/j.earscirev.2016.06.012

Granger, D. E., Kirchner, J. W., & Finkel, R. (1996). Spatially-averaged long term erosion rates measured from in situ-produced cosmogenic nuclides in alluvial sediments. *The Journal of Geology*, *104*, 249–257. https://doi.org/10.2307/256788

Gutierrez, C. I., Tan, S. S., & Clahan, K. B. (2008). Preliminary geologic map of the east half Santa Barabara 30' x 60' quadrangle, California. *California Geological Survey Regional Geologic Map Series, 1:100,000 Scale*, 1.

Hack, J. T. (1975). Dynamic equilibrium and landscape evolution. *Theories of Landform Development: Publications in Geomorphology*. Retrieved from http://geomorphology.sese.asu.edu/Papers/Hack_1975.pdf

Heimsath, A. M., & Whipple, K. X. (2019). Strength Matters: Resisting Erosion Across Upland Landscapes. *Earth Surface Processes and Landforms*. https://doi.org/10.1002/esp.4609

Helmold, K. P., & van de Kamp, P. C. (1984). Diagenetic mineralogy and controls on albitization and laumontite formation in Paleogene Arkoses, Santa Ynez Mountains, California. *AAPG Memoir 37*, *0*(1), 239–276.

Hoek, E., & Brown, E. (1980). Empirical Strength Criterion for Rock Masses. *Journal of the Geotechnical Engineering Division*. https://doi.org/10.1016/0148-9062(81)90766-X

Hoek, E., & Brown, E. (1997). Practical estimates of rock mass strength. *International Journal of Rock Mechanics and Mining Sciences*, *34*(8), 1165–1186. https://doi.org/10.1016/S1365-1609(97)80069-X

Hoek, E., & Marinos, P. (2000). Predicting tunnel squeezing problems in weak heterogeneous rock masses. *Tunnels and Tunnelling International*, *Part 1-2*(November), 1–20. Retrieved from https://www.rocscience.com/documents/hoek/references/H2000d.pdf%0Ahttp://www.rockscience.com/hoek/references/H2000d.pdf

Hoek, E., Carranza, C., & Corkum, B. (2002). Hoek-brown failure criterion – 2002 edition. *Narms-Tac*, 267–273. https://doi.org/10.1016/0148-9062(74)91782-3

Holbrook, W. S., Riebe, C. S., Elwaseif, M., Hayes, J. L., Basler-Reeder, K., Harry, D. L., et al. (2014). Geophysical constraints on deep weathering and water storage potential in the Southern Sierra Critical Zone Observatory. *Earth Surface Processes and Landforms*, *39*(3),

366–380. https://doi.org/10.1002/esp.3502

Howard, J. L. (1988). Sedimentation of the Sespe Formation in southern California. *Santa Barbara and Ventura Basins: Tectonics, Structure, Sedimentation, Oil Fields along an East-West Transect.*, *64*(1988), 53–69.

Hughes, A. (2019). *Quaternary structural evolution and seismic hazards of the onshore Ventura basin, southern California, USA*. Imperial College London.

Jaky, J. (1944). The coefficient of earth pressure at rest. *Journal of the Society of Hungarian Architects and Engineers*, 355–358.

Kirkpatrick, H. M., Moon, S., Yin, A., & Harrison, T. M. (2020). Impact of fault damage on eastern Tibet topography. *Geology*, *48*. https://doi.org/10.1130/G48179.1/5137742/g48179.pdf

Korup, O. (2008). Rock type leaves topographic signature in landslide-dominated mountain ranges. *Geophysical Research Letters*, *35*(11), 1–5. https://doi.org/10.1029/2008GL034157

Leone, J. D., Holbrook, W. S., Riebe, C. S., Chorover, J., Ferré, T. P. A., Carr, B. J., & Callahan, R. P. (2020). Strong slope-aspect control of regolith thickness by bedrock foliation. *Earth Surface Processes and Landforms*, *3010*(July), 2998–3010. https://doi.org/10.1002/esp.4947

Leung, C. F., & Radhakrishnan, R. (1990). Geotechnical properties of weathered sedimentary rocks. *Geotechnical Engineering*, *21*(1), 29–48.

Levy, Y., Rockwell, T. K., Shaw, J. H., Plesch, A., Driscoll, N. W., & Perea, H. (2019). Structural Modeling of the Western Transverse Ranges: An Imbricated Thrust Ramp Architecture. *Lithosphere*, 1–38. https://doi.org/10.1130/L1124.1/4860092/l1124.pdf

Marshall, J. A., & Roering, J. J. (2014). Diagenetic variation in the Oregon Coast Range: Implications for rock strength, soil production, hillslope form, and landscape evolution. *Journal of Geophysical Research: Earth Surface*, *119*, 1395–1417. https://doi.org/10.1002/2013JF003004.

Marshall, S. T., Funning, G. J., & Owen, S. E. (2013). Fault slip rates and interseismic deformation in the western Transverse Ranges, California. *Journal of Geophysical Research: Solid Earth*, *118*(8), 4511–4534. https://doi.org/10.1002/jgrb.50312

Marshall, S. T., Funning, G. J., Krueger, H. E., Owen, S. E., & Loveless, J. P. (2017). Mechanical models favor a ramp geometry for the Ventura-pitas point fault, California. *Geophysical Research Letters*. https://doi.org/10.1002/2016GL072289

Martin, A. J., & Diehl, J. G. (2004). Practical Experience Using A Simplified Procedure To Measure Average Shear-Wave Velocity To A Depth Of 30 Meters (Vs30). *13th World Conference on Earthquake Engineering*, (952), 9. Retrieved from http://www.iitk.ac.in/nicee/wcee/article/13_952.pdf

Mayne, P. W., & Kulhawey, F. H. (1982). K0-OCR Relationship in Soil. *Journal of the Soil Mechanics and Foundations Division*, *108*(6), 851–872.

Medwedeff, W. G., Clark, M. K., Zekkos, D., West, A. J., Chamlagain, D., Atwood, A., et al. (2019). Seismic characterization of the Critical Zone in the Nepal Himalaya: a regional perspective. In *American Geophysical Union, Fall Meeting, Abstract #NS21C-0824*.

Molnar, P., Anderson, R. S., & Anderson, S. P. (2007). Tectonics, fracturing of rock, and erosion. *Journal of Geophysical Research: Earth Surface*, *112*(3), 1–12. https://doi.org/10.1029/2005JF000433

Montgomery, D. R., & Brandon, M. T. (2002). Topographic controls on erosion rates in tectonically active mountain ranges. *Earth and Planetary Science Letters*, *201*(3–4), 481–489. https://doi.org/10.1016/S0012-821X(02)00725-2

Moon, V., & Jayawardane, J. (2004). Geomechanical and geochemical changes during early stages of weathering of Karamu Basalt, New Zealand. *Engineering Geology*, *74*(1–2), 57–72. https://doi.org/10.1016/j.enggeo.2004.02.002

Namson, J. S., & Davis, T. L. (1988). Structural transect of the western Transverse Rances, California: Implications for lithospheric kinematics and seismic risk evaluation. *Geology*, *16*, 675–679.

Neely, A. B., DiBiase, R. A., Corbett, L. B., Bierman, P. R., & Caffee, M. W. (2019). Bedrock fracture density controls on hillslope erodibility in steep, rocky landscapes with patchy soil cover, southern California, USA. *Earth and Planetary Science Letters*, *522*, 186–197. https://doi.org/10.1016/j.epsl.2019.06.011

Niemi, N. A., & Clark, M. K. (2018). Long-term exhumation rates exceed paleoseismic slip rates in the central Santa Monica Mountains, Los Angeles County, California. *Geology*, *46*(1), 63–66. https://doi.org/10.1130/G39388.1

Park, C. B., Miller, R. D., & Xia, J. (1998). Imaging dispersion curves of surface waves on multi-channel record. In *Expanded Abstracts: 68th Annual International Meeting, Society of Exploration Geophysicists* (pp. 1377–1380). https://doi.org/10.1190/1.1820161

Park, C. B., Miller, R. D., & Xia, J. (1999). Multichannel analysis of surface waves. *Geophysics*, *64*(3), 800–808. https://doi.org/10.1190/1.1444590

Park, C. B., Miller, R. D., Xia, J., & Ivanov, J. (2000). Multichannel seismic surface-wave methods for geotechnical applications. *Proc. of the First Int. Conf. on the App ….* Retrieved from http://www.kgs.ku.edu/Geophysics2/Pubs/Pubs/PAR-00-03.pdf

Portenga, E. W., Clark, M. K., & Niemi, N. A. (2017). Spatial and Temporal Patterns of Motion Along the Malibu Coastal Fault Inferred from 10Be Erosion Rates. In *American Geophysical Union, Fall Meeting, Abstract #EP32C-02*. New Orleans, LA.

Reiners, P. W., Farley, K. A., & Hickes, H. J. (2002). He diffusion and (U-Th)/He thermochronometry of zircon: Initial results from Fish Canyon Tuff and Gold Butte. *Tectonophysics*, *349*(1–4), 297–308. https://doi.org/10.1016/S0040-1951(02)00058-6

Riebe, C. S., Hahm, W. J., & Brantley, S. L. (2017). Controls on deep critical zone architecture: a historical review and four testable hypotheses. *Earth Surface Processes and Landforms*, *42*(1), 128–156. https://doi.org/10.1002/esp.4052

Rockwell, T. K. (1988). Neotectonics of the San Cayetano fault, Transverse Ranges, California. *Geological Society of America Bulletin*, *100*, 500–513.

Roy, S. G., Koons, P. O., Upton, P., & Tucker, G. E. (2015). The influence of crustal strength fields on the patterns and rates of fluvial incision. *Journal of Geophysical Research : Earth Surface*, *120*, 275–299. https://doi.org/10.1002/2015JF003602.Received

Roy, S. G., Tucker, G. E., Koons, P. O., Smith, S. M., & Upton, P. (2016). A fault runs through it: Modeling the influence of rock strength and grain-size distribution in a fault-damaged landscape. *Journal of Geophysical Research: Earth Surface*, *121*(10), 1911–1930. https://doi.org/10.1002/2015JF003662

Schmidt, K. M., & Montgomery, D. R. (1995). Limits to Relief. *Science*, *270*(5236), 617–620.

Scott, D. N., & Wohl, E. E. (2018). Bedrock fracture influences on geomorphic process and form across process domains and scales. *Earth Surface Processes and Landforms*. https://doi.org/10.1002/esp.4473

Selby, M. J. (1980). A rock mass strength classification for geomorphic purposes: With tests from Antarctica and New Zealand. *Z. Geomorphol*, *24*, 31–51.

Selby, M. J. (1993). *Hillslope materials and processes*. Oxford University Press.

Sklar, L. S., & Dietrich, W. E. (2001). Sediment and rock strength controls on river incision into bedrock. *Geology*, *29*(12), 1087–1090. https://doi.org/10.1130/0091-7613(2001)029<1087:SARSCO>2.0.CO

Slim, M., Perron, J. T., Martel, S. J., & Singha, K. (2015). Topographic stress and rock fracture: A two-dimensional numerical model for arbitrary topography and preliminary comparison with borehole observations. *Earth Surface Processes and Landforms*, *40*(4), 512–529. https://doi.org/10.1002/esp.3646

Stock, J. D., & Montgomery, D. R. (1999). Geologic constraints on bedrock river incision using the stream power law. *Journal of Geophysical Research: Solid Earth*, *104*(B3), 4983–4993. https://doi.org/10.1029/98JB02139

Stokoe, K. H., & Santamarina, J. C. (2000). Seismic-wave-based testing in geotechnical engineering. *Proceedings of the International Society for Rock Mechanics*.

Stokoe, K. H., Wright, S. G., Bay, J. A., & Roesset, J. M. (1994). Characterization of geotechical sites by SASW method. In R. D. Woods (Ed.), *Geophysical Characterization of Sites* (pp. 15–26). New York: International Science.

Townsend, K. F., Clark, M. K., & Niemi, N. A. (2018). Short-term variability versus long-term consistency of inferred fault slip rates in the Western Transverse Ranges, Southern California. In *American Geophysical Union, Fall Meeting, Abstract #T42B-02*. Washington. D.C.

Townsend, K. F., Gallen, S. F., & Clark, M. K. (2020a). Quantifying Near-Surface Rock Strength on a Regional Scale From Hillslope Stability Models. *Journal of Geophysical Research: Earth Surface*, *125*(7). https://doi.org/10.1029/2020JF005665

Townsend, K.F., Clark, M.K., & Zekkos, D. (2020b). Profiles of near-surface rock mass strength across gradients in erosion, burial, and time [Data set]. University of Michigan - Deep Blue. https://doi.org/10.7302/krah-yx31

Vilder, S. J., Brain, M. J., & Rosser, N. J. (2019). Controls on the geotechnical response of sedimentary rocks to weathering. *Earth Surface Processes and Landforms*. https://doi.org/10.1002/esp.4619

de Vilder, S. J., Brain, M. J., & Rosser, N. J. (2019). Controls on the geotechnical response of

sedimentary rocks to weathering. *Earth Surface Processes and Landforms*, *1929*(May), 1910–1929. https://doi.org/10.1002/esp.4619

Von Voigtlander, J., Clark, M. K., Zekkos, D., Greenwood, W. W., Anderson, S. P., Anderson, R. S., & Godt, J. W. (2018). Strong variation in weathering of layered rock maintains hillslope-scale strength under high precipitation. *Earth Surface Processes and Landforms*, *1194*(March), 1183–1194. https://doi.org/10.1002/esp.4290

Wang, H. Y., & Wang, S. Y. (2015). A new method for estimating Vs (30) from a shallow shear-wave velocity profile (depth <30 m). *Bulletin of the Seismological Society of America*, *105*(3), 1359–1370. https://doi.org/10.1785/0120140103

West, A. J., Galy, A., & Bickle, M. (2005). Tectonic and climatic controls on silicate weathering. *Earth and Planetary Science Letters*, *235*(1–2), 211–228. https://doi.org/10.1016/j.epsl.2005.03.020

Western Regional Climate Center. https://wrcc.dri.edu. Accessed [17/04/2020].

Whipple, K. X., Kirby, E., & Brocklehurst, S. H. (1999). Geomorphic limits to climate-induced increases in topographic relief. *Nature*, *401*, 39–43. https://doi.org/10.1038/43375

Willett, S. D., & Brandon, M. T. (2002). On steady state in mountain belts. *Geology*, *30*(2), 175–178. https://doi.org/10.1130/0091-7613(2002)030<0175

Worden, R. H., & Burley, S. D. (2003). Sandstone Diagenesis: The Evolution of Sand to Stone. In *Sandstone Diagenesis: Recent and Ancient* (pp. 3–44). Malden, MA: Blackwell Publishing. https://doi.org/10.1002/9781444304459.ch

Xia, J., Miller, R. D., Park, C. B., & Tian, G. (2003). Inversion of high frequency surface waves with fundamental and higher modes. *Journal of Applied Geophysics*, *52*(1), 45–57. https://doi.org/10.1016/S0926-9851(02)00239-2

Yong, A., Thompson, E. M., Wald, D. J., Knudsen, K. L., Odum, J. K., William J Stephenson, & Haefner, S. (2016). Compilation of Vs30 Data for the United States, 8 p.

Yoon, S., & Rix, G. J. (2009). Near-Field Effects on Array-Based Surface Wave Methods with Active Sources. *Journal of Geotechnical and Geoenvironmental Engineering*, *135(2)*(March), 399–406. https://doi.org/10.1061/(ASCE)1090-0241(2009)135

Tables

Table 1: Mean strength metrics of sandstones by mapped formation in the Topatopa Mountains

Formation	Schmidt[†]	GSI[†]	GSI Structure[†]	GSI Surfaces[†]	τ at 10m Depth[†]	Vs$_{30}$[†]
Age	R	of 100	of 6	of 5	MPa	m/s
Saugus *Plio-Pleistocene*	0	23[‡]	2[‡]	2[‡]	0.15[‡]	-
Pico *Pliocene*	3 ± 4	30 ± 5	2.3 ± 0.4	2.2 ± 0.4	0.19 ± 0.03	361 ± 19
Towsley *Mio-Pliocene*	6 ± 4	30 ± 5	2.6 ± 0.5	2.4 ± 0.4	0.22 ± 0.03	480 ± 65
Sisquoc *Miocene*	14[‡]	33[‡]	4[‡]	4[‡]	0.28[‡]	-
Monterey *Miocene*	29 ± 10	53 ± 17	4.4 ± 1.3	3.4 ± 0.6	0.75 ± 0.26	727 ± 135
Vaqueros *Oligocene*	37 ± 2	45 ± 0	3.5 ± 0.5	3.3 ± 0.3	0.54 ± 0.02	-
Sespe *Oligocene*	32 ± 3	70 ± 8	5.0 ± 0.6	4.1 ± 0.6	1.35 ± 0.55	875 ± 164
Coldwater *Eocene*	31 ± 5	61 ± 11	4.6 ± 0.5	3.8 ± 0.4	0.92 ± 0.39	603 ± 62
Cozy Dell *Eocene*	42 ± 5	55 ± 0	5 ± 0	3.3 ± 0.3	0.84 ± 0.09	-
Matilija *Eocene*	42 ± 12	69 ± 7	5.4 ± 0.4	3.9 ± 0.5	1.78 ± 0.77	1092 ± 213
Juncal *Eocene*	39 ± 6	56 ± 8	4.2 ± 0.6	3.6 ± 0.5	0.86 ± 0.25	572 ± 41
Unnamed *Cretaceous*	48 ± 11	83 ± 8	5.8 ± 0.2	4.7 ± 0.5	5.49 ± 3.66	679[†]

[†] ± indicates 1σ
[‡] only one site measured

Table 2: Mean strength metrics of the Sespe Formation, by location

Location	Schmidt[†]	GSI[†]	GSI Structure[†]	GSI Surfaces[†]	τ at 10m Depth[†]	Vs$_{30}$[†]
	R	of 100	of 6	of 5	MPa	m/s
Topatopa Mountains	32.4 ± 2.8	69.6 ± 7.8	5.0 ± 0.6	4.1 ± 0.6	1.35 ± 0.55	875 ± 164
Santa Monica Mountains	22.1 ± 7.3	62.4 ± 13.2	4.9 ± 1.0	3.6 ± 0.4	0.84 ± 0.43	648 ± 113
Santa Rosa Island	15.3[‡]	50[‡]	4.5[‡]	3[‡]	0.43[‡]	-

[†] ± indicates 1σ
[‡] only one site measured

Table 3: Empirically derived relationships between shear strength and S-wave velocities

Geologic Age	Equation	R^2
Pliocene	$\tau = 0.0012V_s - 0.3325$	0.95
Miocene	$\tau = 0.0016V_s - 0.3869$	0.97
Oligocene	$\tau = 0.0017V_s - 0.2865$	0.96
Eocene to Cretaceous	$\tau = 0.0022V_s - 0.7123$	0.96

Figure Captions

Figure 1: Simplified geology and structure of the Western Transverse Ranges (WTR). Sites from which Schmidt hammer rebound values and GSI observations were collected (Rockmass Characterization) are shown as yellow circles (n = 226), and locations surveyed for S-wave velocities are shown as white rectangles (n = 60). Black rectangles show extent of Figures 2a, 2b, and 2c. Inset map shows location of the WTR in southern California, USA. Shortening across the WTR is driven by convergence associated with the Big Bend in the SAFZ. MTC–Mendocino Triple Junction, SYF–Santa Ynez Fault, SCF–San Cayetano Fault, MCF–Malibu Coast Fault.

Figure 2: S-wave survey locations, rockmass characterization locations, and geologic units by age in the a) Topatopa Mountains, b) Santa Monica Mountains, and c) Santa Cruz and Santa Rosa Islands. Geologic map units with solid colors are sedimentary (predominately sandstones), cross-hatching indicates metamorphic or volcanic (intrusive and extrusive) lithologic types, and dots indicate Quaternary units. F–Fault.

Figure 3: Mean (± 1σ) Schmidt R, GSI, shear strength at 10m depth, and Vs_{30} by lithologic type of all data in the Western Transverse Ranges. Shaded colors indicate sedimentary, igneous, and metamorphic (Meta.) rock types, and open circles indicate that a single measurement was made. For Schmidt R, GSI, and shear strength, 75% of the data is from sandstone units, 15% is from shale units, and 10% is from all other lithologic types. For Vs_{30}, 57% of the data is from sandstone units, 27% of the data is from shale units, and 16% of the data is from all other lithologic types. (n = number of geotechnical characterization sites, *number of Vs profiles*).
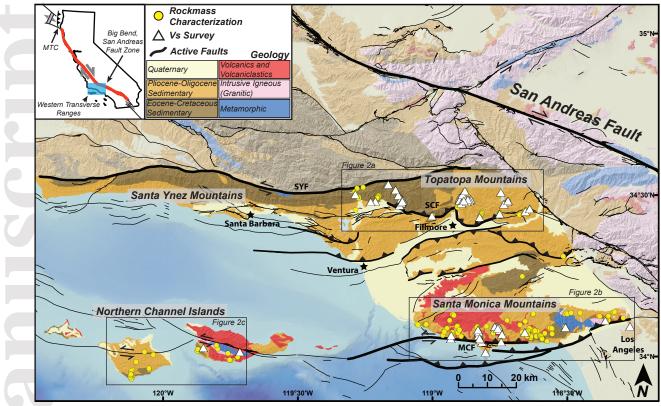
Figure 4: S-wave velocity and shear strength profiles from all sites in the Western Transverse Ranges, colored by lithologic type. Heavy black lines and dashed black lines are the mean and ± 1σ profile of sandstone profiles, and heavy grey lines and dashed grey lines are the mean and ± 1σ profile of shale profiles. Sandstone and shale sites demonstrate considerable variability in sub-surface S-wave velocities and shear strength, whereas sites overlying all other lithologic types measured, including unconsolidated fill, conglomerate, volcanic and volcaniclastic units, granitoids, schists, and slate generally yield S-wave velocities and shear strength on the low end of the ranges of sandstone and shale. Note that sandstone and shale shear strength profiles at < 1 MPa are obscured by other lithologic types at these low strength values.

Figure 5: GSI, S-wave velocity profiles, and shear strength profiles of sandstone units in the Topatopa Mountains. Data are arranged by the stratigraphic age of the unit from which the data was collected. S-wave and shear strength profiles are colored by the geomorphic position of the site.
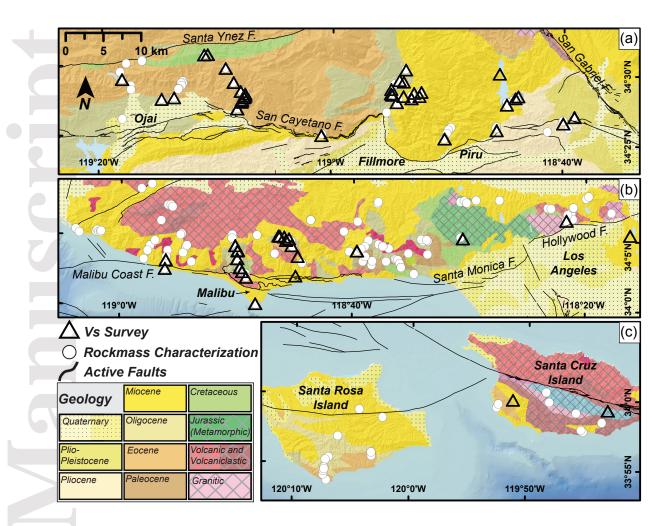
Figure 6: Mean Schmidt hammer rebound values, mean GSI, and mean Vs_{30} of sandstone sites by geologic unit in the Topatopa Mountains. Bars indicate ± 1σ variability about means, and data without error bars represent a single measurement. Geologic units are arranged from youngest (Plio-Pleistocene) to oldest (Cretaceous). Mean Schmidt hammer rebound values, GSI, and Vs_{30} on sandstone increase with increasing age from Plio-Pleistocene (Saugus) to Oligocene (Sespe). Mean Schmidt hammer rebound values are largely the same for Eocene and Cretaceous units, whereas mean Vs_{30} is variable for these units.

Figure 7: S-wave velocity profiles and shear strength profiles of the Oligocene Sespe Formation (sandstone units) in the Santa Monica Mountains and Topatopa Mountains.

Figure 8: Mean shear strength against mean S-wave velocity profiles of all data from the Western Transverse Ranges, calculated in 3m intervals. Data are separated into four relationships by geologic age, which define linear trends. Dashed black lines indicate linear regressions through each of the four relationships, which are reported in Table 3. Error bars are standard error.

Figure 9: Mean strength metrics ($\pm$ 1σ) of the Sespe Formation, including Schmidt hammer R, GSI, Vs_{30}, and shear strength against erosion rates inferred from a) [10]Be catchment-averaged cosmogenic radionuclides, and b) apatite and zircon (U-Th)/He low-temperature thermochronometry. There are no $\pm$ 1σ bars about Santa Rosa Island values because only one data point was collected. Note that strength metrics are offset from true erosion rate by up to ~0.1 mm/yr for visibility.

S-wave Velocity (m/s)

Shear Strength (MPa)

Topatopas
Profile
Mean
± 1σ
Santa Monicas
Profile
Mean
± 1σ

(a) *Cosmogenic Radionuclides*

Topatopa Mountains

Santa Monica Mountains

- Schmidt R
- GSI
- Vs$_{30}$
- Shear Strength

(b) *Low-Temperature Thermochronology*

Topatopa Mountains

Santa Monica Mountains

Santa Rosa Island

- Schmidt R
- GSI
- Vs$_{30}$
- Shear Strength